

Role of nonlocality in exchange-correlation for magnetic two-dimensional van der Waals materials

Y. Lee,¹ Takao Kotani,² and Liqin Ke^{1,*}

¹Ames Laboratory, U.S. Department of Energy, Ames, Iowa 50011, USA

²Department of Applied Mathematics and Physics, Tottori University, Tottori 680-8552, Japan

(Dated: June 9, 2020)

To obtain accurate independent-particle descriptions for ferromagnetic two-dimensional van der Waals materials, we apply the quasiparticle self-consistent GW (QSGW) method to VI_3 , CrI_3 , CrGeTe_3 , and Fe_3GeTe_2 . QSGW provides a description of the nonlocal exchange-correlation term in the one-particle Hamiltonian. The nonlocal term is important not only as the U of density functional theory (DFT)+ U but also for differentiating occupied and unoccupied states in semiconductors. We show the limitations of DFT+ U in mimicking QSGW.

Introduction.— The recent experimental realization of magnetic two-dimensional (2D) van der Waals (vdW) materials has generated great interest for exploiting novel 2D magnetism and for applications such as energy-efficient ultracompact spin-based electronics [1]. Long-range ferromagnetic ordering in the atomically thin systems was first demonstrated in the CrGeTe_3 bilayer [2] and CrI_3 monolayer [3], albeit only at very low temperatures. Later, Deng *et al.* [4] showed that an electric field could drastically increase the Curie temperature, T_C , of a Fe_3GeTe_2 monolayer up to room temperature. Recently, VI_3 has been identified as the first vdW hard ferromagnet with a large coercivity [5–7]. Spurred by these experiments, many theoretical efforts have been published treating magnetic 2D vdW materials (m2Dv) [8–15].

We are also witnessing the recent revolutionary development of materials informatics (MI). For example, Mounet *et al.* [16] have employed a computational MI to search for 2D exfoliable materials by multi-level screening from the databases of experimentally known compounds. The quality of such work largely depends on the choice of the first-principles method used for the final screening. In the future, such an MI procedure may be applied to m2Dv. Then the first-principles method used in MI should be as reliable as possible and with no adjustable parameters for each material.

Until now, m2Dv has been theoretically treated mostly within density functional theory (DFT)+ U , with a single Hubbard U applied on the cation- $3d$ orbitals, as in Refs.[17–20]. Phenomenological theories, such as DFT+ U and dynamical mean-field theory, are very useful for various material systems. However, it is not clear that one can use DFT+ U for the above-mentioned MI, because of the limitation of the single parameter U , as we illustrate in the following.

First, the cation- $3d$ bands in m2Dv contain more degrees of freedom than a single U parameter can describe. Although DFT+ U may adjust overall splitting between occupied and unoccupied $3d$ bands for each spin, it ignores the k dependence and frequency dependence of ef-

fective interactions and thus the interaction anisotropy regarding in-plane and out-of-plane $3d$ orbitals in m2Dv can not be adequately treated. An idea using many parameters for the U term would be hard to implement because of the difficulty in determining the unique parameters.

Second, the relative positions of cation- $3d$ and anion- p bands are not directly controlled by onsite U . For example, even in nonmagnetic CdO where we expect no U effect because $\text{Cd-}4d$ states are fully occupied, we see the center of occupied $4d$ states can be pushed down about 2 eV (see Fig. A1 in Ref. [21]) in comparison with DFT. Note that the relative positions of and hybridizations between cation- $3d$ and anion- p can be important to determine the super-exchange coupling in m2Dv.

In this Rapid Communication, we apply the quasiparticle self-consistent GW (QSGW) method [21–23] to m2Dv, including VI_3 , CrI_3 , CrGeTe_3 , and Fe_3GeTe_2 . QSGW has been applied to a wide range of materials and shown to be the most reliable method available to determine the one-particle Hamiltonian H_0 , which defines the independent-particle picture of a particular material. For each material, an accurate H_0 is the key to evaluate all of its physical quantities theoretically. We will show that QSGW reasonably describes electronic structures consistent with experiments for all m2Dv treated here. Then we will examine whether DFT+ U can mimic the band structures obtained in QSGW. We will demonstrate the serious limitations of DFT in treating m2Dv, corresponding to the two reasons discussed above.

Methods.— First, let us recall the GW approximation (GWA) [24, 25]. GWA can be applied to any one-particle Hamiltonian H_0 , for example, to the Kohn-Sham Hamiltonian of DFT. In GWA, we calculate the self-energy $\Sigma(\mathbf{r}, \mathbf{r}', \omega) = \Sigma(1, 2) = iG_0(1, 2)W(1+, 2)$. Here $G_0 = 1/(\omega - H_0)$ is the Green's function of H_0 ; W is the dynamically screened Coulomb interaction calculated using G_0 , usually in the random phase approximation (RPA). Then we can determine the quasiparticle energies with $\Sigma(\mathbf{r}, \mathbf{r}', \omega)$ in the place of the exchange-correlation (xc) potential. The reliability of this one-shot method, so-called G_0W_0 , depends on the reliability of H_0 .

Thus, the main theoretical problem of G_0W_0 is how to

* Corresponding author: liqinke@ameslab.gov

determine H_0 to which we apply GWA. For this purpose, various self-consistent schemes have been developed. In practice, a partial self-consistency is often employed due to the demanding nature of computation or the intrinsic problems of the methods [26]. In the so-called energy-only self-consistent GW method [27, 28], the eigenfunctions are fixed while only the one-particle energies are iterated to reach consistency. In a GW_0 method [28], one may calculate W using DFT G_0 , but iterate G until convergence.

QSGW [22, 23, 29] is given as a self-consistent perturbation method based on the quasiparticle picture within GWA. The full many-body Hamiltonian H is divided into $H = H_0 + (H - H_0)$, then $(H - H_0)$ is treated as a perturbation in GWA. The self-consistent perturbation requires that we should determine H_0 so that the term generated in GWA due to $(H - H_0)$ gives virtually zero.

Based on this idea, we generate the QSGW xc potential $V_{\text{QSGW}}^{\text{xc}}$ from the self-energy $\Sigma(\mathbf{r}, \mathbf{r}', \omega)$ obtained in GWA as

$$V_{\text{QSGW}}^{\text{xc}} = \frac{1}{2} \sum_{ij} |\psi_i\rangle \{ \text{Re}[\Sigma(\epsilon_i)]_{ij} + \text{Re}[\Sigma(\epsilon_j)]_{ij} \} \langle \psi_j|. \quad (1)$$

Here ϵ_i and $|\psi_i\rangle$ are eigenvalues and eigenfunctions, respectively, of Hamiltonian H_0 . Re denotes the Hermitian part. $\Sigma_{ij}(\omega) = \langle \psi_i | \Sigma(\omega) | \psi_j \rangle = \int d^3\mathbf{r} \int d^3\mathbf{r}' \psi_i^*(\mathbf{r}) \Sigma(\mathbf{r}, \mathbf{r}', \omega) \psi_j(\mathbf{r}')$. With Eq.(1), we have a mapping to generate a new H_0 , $H_0^{(i)} \rightarrow H_0^{(i+1)}$. This is repeated until H_0 is converged. Note that G_0W_0 applied to this self-consistent H_0 does not cause corrections of the quasiparticle energies because of this self-consistency.

QSGW, as it is, tends to systematically overestimate exchange effects, especially for bandgaps [21, 22, 30]. This can be due to the underestimation of the screening effect in RPA, which neglects electron-hole correlations in the proper polarization function [28, 30], and/or the neglect of the screening effect of phonons [31]. Shishkin *et al.* [28] performed calculations that include the correlation via the vertex correction for W and demonstrated very reliable predictions of band gaps by recovering the screening underestimation. However, their methods are too computationally demanding to apply to the materials treated here. Based on the observation that the underestimations are rather systematic in various systems [32], we here use a hybrid QSGW method, QSGW80 [21, 33], which uses an empirical mixing of $V^{\text{xc}} = 0.8V_{\text{QSGW}}^{\text{xc}} + 0.2V_{\text{LDA}}^{\text{xc}}$. QSGW80 is taken to be a substitution of the method by Shishkin *et al.* to remedy the underestimation quickly and efficiently. Unless specified, all QSGW calculations in this work are carried out in QSGW80, referred to hereafter as QSGW, for simplicity.

The nonlocality of $V_{\text{QSGW}}^{\text{xc}}$ provides a natural description of the correct independent-particle picture. Generally speaking, we can classify this nonlocality into two parts: on site and off site. The on-site nonlocality, which can differentiate five $3d$ orbitals, can be approximated, to

a certain extent, by the Hubbard U in DFT+ U . The off-site nonlocality is critical to generate bandgaps in semiconductors. To illustrate this, let us consider a hydrogen dimer H_2 . To lower the highest occupied molecular orbital (HOMO) energy without changing the shape of eigenfunctions, one needs to introduce a projector of HOMO. The corresponding projector is naturally represented by a nonlocal potential, and the screened exchange contribution in $V_{\text{QSGW}}^{\text{xc}}$ works exactly as such a projector.

Furthermore, in contrast to the hybrid functional methods, the electron screening effects on the exchange is calculated explicitly in QSGW. The screened Coulomb interaction W , which determines the screened exchange, is spatially dependent and self-consistently determined without any system-dependent parameters. On the other hand, in the hybrid functional methods such as Heyd-Scuseria-Ernzerhof (HSE), the xc functional is obtained by mixing the DFT xc with the Hartree-Fock (HF) exchange, which is calculated using the bare Coulomb interaction kernel. The mixing parameter solely mimics the screening effect. This limits the universality of the hybrid functional methods because the screening effects vary significantly between metals and semiconductors, and their spatial dependence could be important in anisotropic systems, which can be hard to be mimicked by one single parameter. In fact, He and Franchini [34] showed that the mixing could be very material-dependent. Thus, the explicit treatment of screened exchange allows QSGW to treat complex subjects such as metal/insulator interfaces, and also m2Dv, which contain both features of semiconductor and anisotropic magnetic materials.

Computational details.— We use the QSGW method from the ECALJ package [23], which is implemented with a mixed basis and allows automatic interpolation of self-energy in the whole Brillouin zone without resorting to the WANNIER90 techniques [35, 36]. The spin-orbit coupling (SOC) is included as a perturbation [21] after we attain the self-consistency of QSGW. We employed the experimental lattice parameters [5, 37–39] for calculations. As for DFT+ U , we use both fully-localized-limit (FLL) [40] and around-the-mean-field (AMF) [41] double-counting schemes to investigate the dependence of band structures on the correlation parameter U , which is applied on the cation- $3d$ orbitals. All DFT and DFT+ U calculations are carried out within the generalized gradient approximation using the functional of Perdew, Burke, and Ernzerhof (PBE) [42].

Results.— Fe_3GeTe_2 is a metallic m2Dv and has a higher T_C than its semiconducting counterparts [4]. Figure 1 shows the total density of states (DOS) and partial density of states (PDOS) calculated in QSGW. DOS obtained by DFT is also shown for comparison. Both QSGW and DFT suggest that Fe_3GeTe_2 is a metal, as found in experiments. DOS are dominated by Fe- $3d$ states in this energy window. The Fermi level E_F is located at a pseudogap of Fe $_1$ - $3d$ states in the minority-spin channel. QSGW gives slightly narrower $3d$ bands than DFT, suggesting a somewhat stronger localization

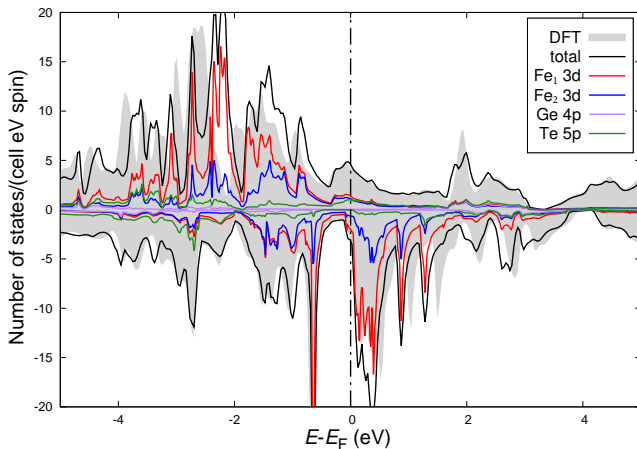


FIG. 1. Total and atom-resolved partial density of states calculated using QSGW in Fe_3GeTe_2 . For comparison, DOS obtained by DFT is shown (shaded area). Spin-orbit coupling is not included.

of electron states in QSGW. Indeed, such $3d$ -band narrowing is rather general in QSGW as shown in Refs. [43 and 44]. Considering the fact that QSGW describes metals such as bcc Fe and also transition-metal oxides such as NiO very well, our result supports the applicability of DFT to Fe_3GeTe_2 . For a band structure comparison between DFT and QSGW, see the Supplemental Material [45].

Note the difficulty of hybrid functionals such as HSE applied to m2Dv without a choice of material-dependent parameters. For example, one usually uses a mixing parameter $a = 0.25$ for semiconductors. However, it was found that $a = 0.15$ [46] is optimum for transition-metal oxides. Furthermore, $a = 0$ is apparently good for bcc Fe while HSE06 gives a magnetic moment of $2.89 \mu_B/\text{Fe}$ [47]. Since semiconducting and metallic features coexist with transition metals in m2Dv, we can hardly expect HSE to work well for m2Dv. We think that QSGW is the optimal choice to describe electronic structures of m2Dv along the line of MI.

Table I summarizes the experimental and our calculated E_g values in m2Dv. Unlike DFT, QSGW correctly predicts VI_3 as a semiconductor. It is worth noting that G_0W_0 applied to DFT does not open the gap in VI_3 , as it does in VO_2 , demonstrating the necessity of self-consistency of GW calculations as in QSGW. For CrGeTe_3 , QSGW gives $E_g = 0.66 \text{ eV}$, within the range of reported experimental values of $0.20\text{--}0.74 \text{ eV}$, while DFT gives a much smaller value of $E_g = 0.19 \text{ eV}$. On the other hand, in CrI_3 , QSGW gives $E_g = 1.68 \text{ eV}$, 35% larger than the only reported experimental value of 1.2 eV . This difference is somewhat larger than expected, considering that QSGW produces E_g within $\sim 10\%$ difference for a wide range of materials [21].

SOC reduces the calculated E_g in all three semiconducting compounds, as shown in Table I, especially within QSGW. The strong SOC effects on E_g are

TABLE I. Bandgaps E_g (eV) calculated in DFT and QSGW, with and without SOC. Experimental values are listed to compare. The reported theoretical E_g are in the range of $0.74\text{--}1.6$, $0\text{--}0.43$, and $0\text{--}1.0 \text{ eV}$ for bulk CrI_3 [10, 48], CrGeTe_3 [9, 13], and VI_3 [6, 20] respectively.

Compound	Experiment	DFT	QSGW	DFT	QSGW
		SOC	SOC	SOC	SOC
VI_3	$0.32\text{--}0.67^{\text{a}}$	0	0.53	0	0.75
CrI_3	1.2^{b}	0.78	1.68	1.07	2.23
CrGeTe_3	$0.20\text{--}0.74^{\text{c}}$	0.19	0.66	0.42	0.99

^a Resistivity measurement: 0.32 eV [20]; optical reflectance: 0.6 eV [7]; optical transmittance: 0.67 eV [20].

^b Optical transition measurement [49].

^c Angle-resolved photoemission spectroscopy (ARPES) measurements: 0.38 eV [50] and 0.2 eV [51]; resistivity measurement: 0.2 eV [52]; scanning tunneling microscopy (STM) measurement: 0.74 eV [18].

due to the heavy anion atoms in the compounds. I- and Te- $5p$ orbitals have rather large SOC constants, $\xi_p = 0.9\text{--}1.0 \text{ eV}$, while V- and Cr- $3d$ orbitals have $\xi_d = 20\text{--}30 \text{ meV}$. The contribution of SOC to E_g of CrI_3 in QSGW (0.55 eV) is about twice as large as in DFT (0.29 eV).

CrI_3 .— Figures 2(a) and 2(b) show the PDOS of CrI_3 calculated in DFT and QSGW, respectively, without SOC. QSGW shifts up the unoccupied states in both spin channels, resulting in a larger E_g than the one we obtain in DFT. In the majority spin, the valence cation- $3d$ states are pushed down relative to the anion- $5p$ states, and the top of valence bands at Γ becomes more dominated by anion- p states.

Figure 2(c) compares the QSGW band structures of CrI_3 calculated with and without SOC. It clearly shows that SOC pushes up top valence bands around the Γ point, resulting in a smaller E_g . Within QSGW, the top of majority-spin valence bands become more pure anion- p -like after $3d$ states are pushed down. As a result, SOC has a stronger effect on decreasing E_g in QSGW than in DFT. Similar SOC effects are also found in VI_3 and CrGeTe_3 .

VI_3 .— QSGW predicts that VI_3 is a semiconductor while DFT incorrectly predicts it as a half metal. E_g obtained in QSGW is within the range of experimental values. Figure 3 shows the PDOS of VI_3 calculated within DFT, DFT+ U , and QSGW. VI_3 has one less electron than CrI_3 in the formula unit. Within DFT, the Fermi level intersects the majority-spin t_{2g} states, resulting in a metallic state. The t_{2g} states consist of five roughly equally occupied $3d$ orbitals. In contrast, remarkably, QSGW splits the d_{z^2} states out of the occupied t_{2g} states and shifts them above E_F . Correspondingly, the remaining t_{2g} states become more occupied, and a bandgap forms between the d_{z^2} states and the other t_{2g} states in the majority spin. Other unoccupied $3d$ states also shift upward for both spins within QSGW.

By adjusting U , DFT+ U can reproduce QSGW E_g in

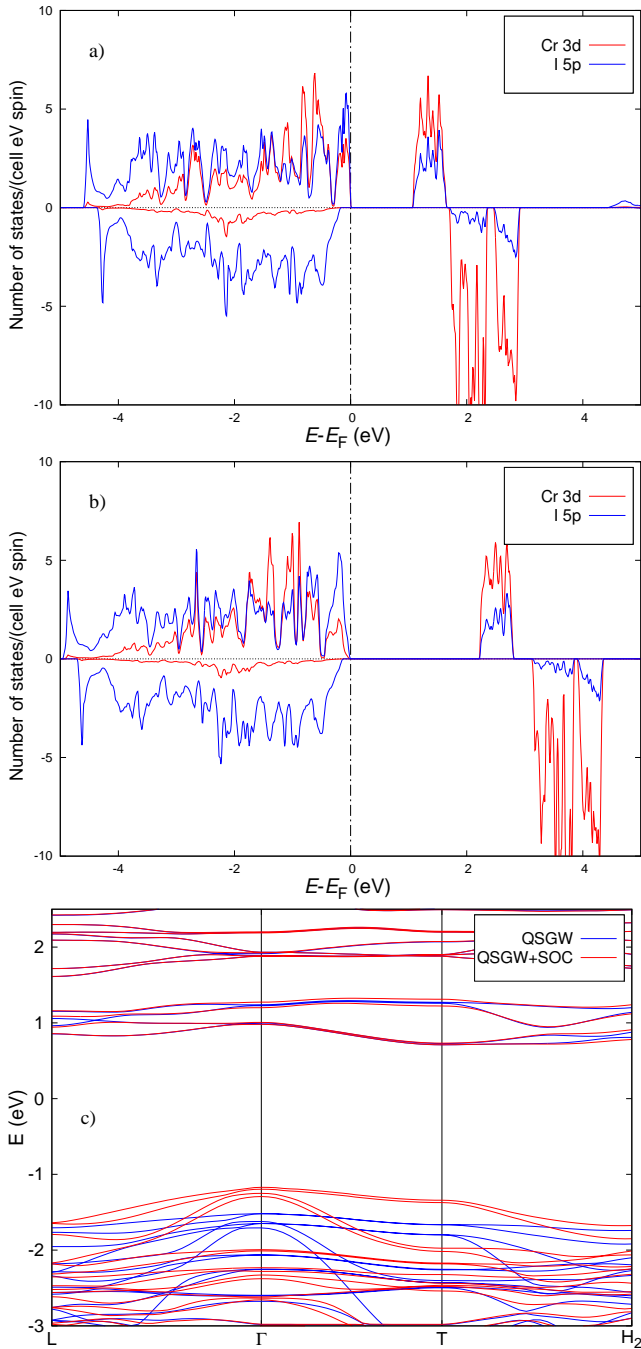


FIG. 2. The partial density of states projected on Cr-3d and I-5p states in CrI₃ calculated within (a) DFT and (b) QSGW. (c) QSGW band structures of CrI₃ calculated with (red) and without (blue) SOC.

VI₃. However, as shown in Fig. 3, a $U = 2.7$ eV may give similar positions of V-3d DOS as in QSGW in the majority spin, but not in the minority one. Moreover, the shapes of occupied majority-spin DOS change significantly in DFT+ U , comparing those in QSGW and in DFT.

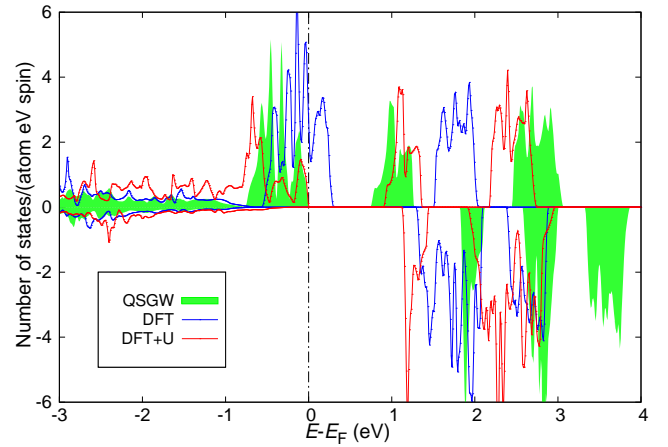


FIG. 3. The partial density of states projected on the V-3d states in VI₃ within DFT (green shaded), DFT+ U , and QSGW. DFT+ U calculation is performed using the AMF scheme. $U = 2.7$ eV is used so that the majority-spin V-3d states peak at similar positions as in QSGW. SOC is not included.

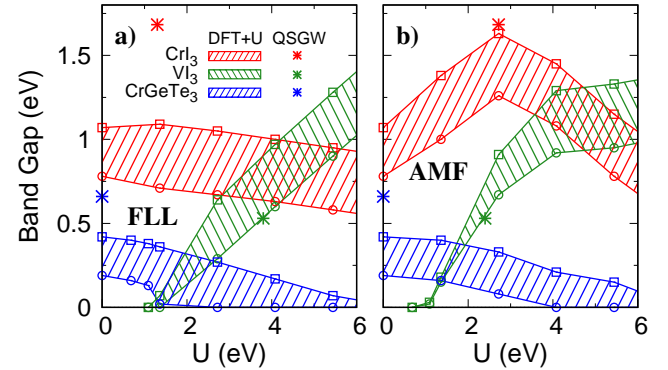


FIG. 4. E_g as a function of U in CrI₃, VI₃, and CrGeTe₃, calculated using the (a) fully-localized-limit scheme (FLL) and (b) around-the-mean-field (AMF) scheme. The lower bound (open circles) and upper bound (open squares) of the shaded areas correspond to calculations with and without SOC, respectively. QSGW+SOC results are included to compare.

DFT+ U .— Figure 4 shows E_g values calculated using two DFT+ U schemes, FLL and AMF, as a function of U , with and without SOC. FLL and AMF give different U dependences of E_g . Within FLL, E_g values of CrI₃ and CrGeTe₃ decrease with increasing U , deviating further from experiments. In VI₃, DFT+ U is not able to produce the experimental semiconducting state, especially with SOC, unless a sufficiently large U is applied, e.g., 2–3 eV in AMF and 3–4 eV in FLL, respectively. Within AMF, E_g values reach the maximum values with $U = 2.7$ and 6.8 eV in CrI₃ and VI₃, respectively, and then decrease. In contrast to VI₃ and CrI₃, E_g of CrGeTe₃ decreases with the increasing of U value in both schemes. Hence, DFT+ U is unable to increase E_g in CrGeTe₃.

To understand the behavior of E_g dependence on U , we examine how electronic structures evolve with the

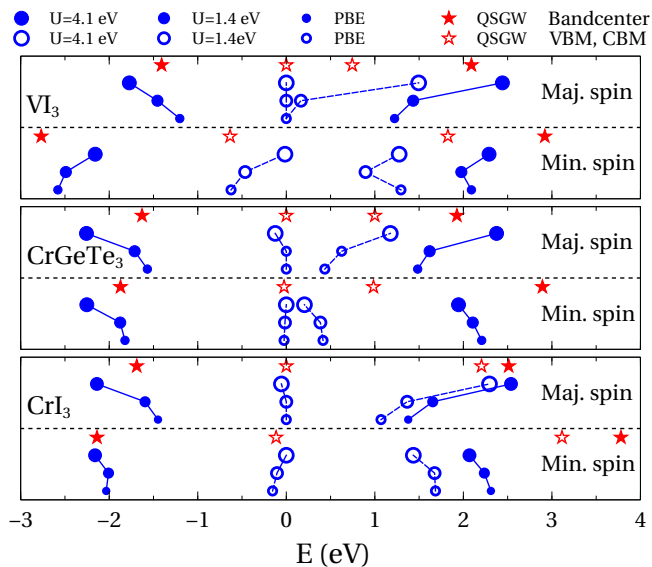


FIG. 5. The CBM, VBM, and centers of $3d$ states in m2Dv in both spin channels calculated in DFT+ U and QSGW. Band centers are denoted by solid circles (DFT+ U) or stars (QSGW) while CBM and VBM are denoted by open circles (DFT+ U) or stars (QSGW). The small, medium, and large circles represent $U = 0, 1.4,$ and 4.1 eV, respectively. The AMF scheme is used for DFT+ U calculation. SOC is not included.

increasing of U in AMF. Figure 5 shows the U dependence of the valence band maximum (VBM), the conduction band minimum (CBM), and the band centers of valence and conduction cation- $3d$ states in both spin channels, comparing with QSGW results. For all three compounds, applying U increases the gap and the distance between the centers of occupied and unoccupied $3d$ bands in the majority-spin but not the minority-spin channel. This is clearly shown in Fig. 3 for the case of VI_3 with $U = 2.7$ eV. In CrI_3 and CrGeTe_3 , a large U pushes up the unoccupied $3d$ bands in the majority spin but lowers them in the minority spin. When U is sufficiently large, the unoccupied $3d$ states in the minority spin are shifted below those in the majority spin, and E_g is determined by the exchange splitting instead of crystal-field splitting. A similar trend is also observed in VI_3 , but it occurs at a much larger U . DOS calculated within DFT, DFT+ U , and QSGW can be found in the Supplemental Material [45].

Can we mimic QSGW DOS by applying U on cation- d orbitals? Now we compare DFT+ U with QSGW DOS. As shown in Fig. 5, QSGW separates further, in comparison to DFT, the occupied and unoccupied states in both spin channels, while DFT+ U only separates them in one spin channel. Hence, within DFT+ U , a single U parameter is not able to mimic the QSGW $3d$ band centers simultaneously in both spin channels. We also apply different J values in DFT+ $U+J$ calculations and are not able to reproduce QSGW $3d$ states in a satisfactory fashion as well. (Results of VI_3 are shown in Fig. S10 in the

Supplemental Material.) Furthermore, VBM and CBM are the bonding and anti-bonding states made of cation- $3d$ and anion- $5p$ orbitals. The positions of unoccupied cation- $3d$ bands relative to anion- $5p$ bands at VBM are not directly controlled by on-site U , which adjusts only occupied $3d$ bands, but by the off-site nonlocal potential that was naturally included in $V_{\text{QSGW}}^{\text{xc}}$ within QSGW. Thus, there is no way that the DFT+ U can be used to mimic QSGW for these systems. It would be interesting to see whether extended Hubbard models, such as DFT+ $U+V$ [53], can satisfactorily approximate such off-site correlations, especially with parameters determined systematically and automatically.

Although QSGW and DFT give the same or similar magnetic moments for all m2Dv we studied here, we expect different exchange couplings calculated in two methods, considering QSGW's profound effects on electronic structures. The anion- $5p$ weights at the top of valence bands are very different within two methods, suggesting that the corresponding superexchange couplings should differ as well.

Finally, QSGW is much more computational demanding in comparison with DFT. Its efficiency needs to be improved for application to large-scale high-throughput calculations. Recently, progress has been made in this direction. For example, self-consistent GW calculations using large unit cells with more than 50 atoms has become feasible [54]. By optimizing algorithms for the polarizability and the self-energy, Kutepov [54] has shown the scaling of computational time is between linear and quadratic with respect to the system size, demonstrating the promising potential of its application on high-throughput computations.

Conclusions.— We investigated the effects of the nonlocal exchange-correlation on the electronic structures of magnetic 2D van der Waals materials using the QSGW method. QSGW correctly predicts the semiconducting states of VI_3 while DFT and G_0W_0 fail. The corresponding calculated values are within the range of reported experimental values for CrGeTe_3 and VI_3 , but larger than the experimental E_g for CrI_3 . We also demonstrated that the simplistic DFT+ U method could not mimic the effects introduced by QSGW, suggesting the importance of a more elaborate treatment of electron correlations in these systems. Furthermore, considering the limitation of the DFT+ U method, the parameter-free and more universal QSGW method is more suitable to work as an engine in MI, providing a good independent-particle picture for high-throughput computations to search for new m2Dv.

ACKNOWLEDGMENTS

This work was supported by the U.S. Department of Energy, Office of Science, Office of Basic Energy Sciences, Materials Sciences and Engineering Division, and Early Career Research Program. Ames Laboratory is operated

for the U.S. Department of Energy by Iowa State University under Contract No. DE-AC02-07CH11358. This research used resources of the National Energy Research Scientific Computing Center (NERSC), a U.S. Department of Energy Office of Science User Facility operated

under Contract No. DE-AC02-05CH11231. T. K. acknowledges the support from JSPS KAKENHI through Grant No. 17K05499, and the computing time provided by Research Institute for Information Technology (Kyushu University).

-
- [1] D. Zhong, K. L. Seyler, X. Linpeng, R. Cheng, N. Sivadas, B. Huang, E. Schmidgall, T. Taniguchi, K. Watanabe, M. A. McGuire, W. Yao, D. Xiao, K.-M. C. Fu, and X. Xu, Van der Waals engineering of ferromagnetic semiconductor heterostructures for spin and valleytronics, *Science Advances* **3**, e1603113 (2017).
- [2] C. Gong, L. Li, Z. Li, H. Ji, A. Stern, Y. Xia, T. Cao, W. Bao, C. Wang, Y. Wang, Z. Q. Qiu, R. J. Cava, S. G. Louie, J. Xia, and X. Zhang, Discovery of intrinsic ferromagnetism in two-dimensional van der Waals crystals, *Nature* **546**, 265 (2017).
- [3] B. Huang, G. Clark, E. Navarro-Moratalla, D. R. Klein, R. Cheng, K. L. Seyler, D. Zhong, E. Schmidgall, M. A. McGuire, D. H. Cobden, W. Yao, D. Xiao, P. Jarillo-Herrero, and X. Xu, Layer-dependent ferromagnetism in a van der Waals crystal down to the monolayer limit, *Nature* **546**, 270 (2017), letter.
- [4] Y. Deng, Y. Yu, Y. Song, J. Zhang, N. Z. Wang, Z. Sun, Y. Yi, Y. Z. Wu, S. Wu, J. Zhu, J. Wang, X. H. Chen, and Y. Zhang, Gate-tunable room-temperature ferromagnetism in two-dimensional Fe_3GeTe_2 , *Nature* **563**, 94 (2018).
- [5] S. Tian, J.-F. Zhang, C. Li, T. Ying, S. Li, X. Zhang, K. Liu, and H. Lei, Ferromagnetic van der Waals Crystal VI_3 , *Journal of the American Chemical Society* **141**, 5326 (2019).
- [6] J. He, S. Ma, P. Lyu, and P. Nachtigall, Unusual Dirac half-metallicity with intrinsic ferromagnetism in vanadium trihalide monolayers, *J. Mater. Chem. C* **4**, 2518 (2016).
- [7] T. Kong, K. Stolze, E. I. Timmons, J. Tao, D. Ni, S. Guo, Z. Yang, R. Prozorov, and R. J. Cava, VI_3 —a New Layered Ferromagnetic Semiconductor, *Advanced Materials* **31**, 1808074 (2019).
- [8] S. Baidya, J. Yu, and C. H. Kim, Tunable magnetic topological insulating phases in monolayer CrI_3 , *Phys. Rev. B* **98**, 155148 (2018).
- [9] Y. Fang, S. Wu, Z.-Z. Zhu, and G.-Y. Guo, Large magneto-optical effects and magnetic anisotropy energy in two-dimensional $\text{Cr}_2\text{Ge}_2\text{Te}_6$, *Phys. Rev. B* **98**, 125416 (2018).
- [10] P. Jiang, L. Li, Z. Liao, Y. X. Zhao, and Z. Zhong, Spin Direction-Controlled Electronic Band Structure in Two-Dimensional Ferromagnetic CrI_3 , *Nano Letters* **18**, 3844 (2018), pMID: 29783842.
- [11] V. V. Kulish and W. Huang, Single-layer metal halides MX_2 ($X = \text{Cl}, \text{Br}, \text{I}$): stability and tunable magnetism from first principles and Monte Carlo simulations, *J. Mater. Chem. C* **5**, 8734 (2017).
- [12] N. Sivadas, S. Okamoto, X. Xu, C. J. Fennie, and D. Xiao, Stacking-Dependent Magnetism in Bilayer CrI_3 , *Nano Letters* **18**, 7658 (2018).
- [13] G. Menichetti, M. Calandra, and M. Polini, Electronic structure and magnetic properties of few-layer $\text{Cr}_2\text{Ge}_2\text{Te}_6$: the key role of nonlocal electron–electron interaction effects, *2D Materials* **6**, 045042 (2019).
- [14] D. Torelli and T. Olsen, Calculating critical temperatures for ferromagnetic order in two-dimensional materials, *2D Materials* **6**, 015028 (2018).
- [15] J. L. Lado and J. Fernández-Rossier, On the origin of magnetic anisotropy in two dimensional CrI_3 , *2D Materials* **4**, 035002 (2017).
- [16] N. Mounet, M. Gibertini, P. Schwaller, D. Campi, A. Merkys, A. Marrazzo, T. Sohier, I. E. Castelli, A. Cepellotti, G. Pizzi, and N. Marzari, Two-dimensional materials from high-throughput computational exfoliation of experimentally known compounds, *Nature Nanotechnology* **13**, 246 (2018).
- [17] S. W. Jang, M. Y. Jeong, H. Yoon, S. Ryee, and M. J. Han, Microscopic understanding of magnetic interactions in bilayer CrI_3 , *Physical Review Materials* **3**, 031001 (2019).
- [18] Z. Hao, H. Li, S. Zhang, X. Li, G. Lin, X. Luo, Y. Sun, Z. Liu, and Y. Wang, Atomic scale electronic structure of the ferromagnetic semiconductor $\text{Cr}_2\text{Ge}_2\text{Te}_6$, *Science Bulletin* **63**, 825 (2018).
- [19] X. Li and J. Yang, CrXTe_3 ($X = \text{Si}, \text{Ge}$) nanosheets: two dimensional intrinsic ferromagnetic semiconductors, *J. Mater. Chem. C* **2**, 7071 (2014).
- [20] S. Son, M. J. Coak, N. Lee, J. Kim, T. Y. Kim, H. Hamidov, H. Cho, C. Liu, D. M. Jarvis, P. A. C. Brown, J. H. Kim, C.-H. Park, D. I. Khomskii, S. S. Saxena, and J.-G. Park, Bulk properties of the van der Waals hard ferromagnet VI_3 , *Phys. Rev. B* **99**, 041402 (2019).
- [21] D. Deguchi, K. Sato, H. Kino, and T. Kotani, Accurate energy bands calculated by the hybrid quasiparticle self-consistent *GW* method implemented in the ECALJ package, *Japanese Journal of Applied Physics* **55**, 051201 (2016).
- [22] T. Kotani, M. van Schilfhaarde, and S. V. Faleev, Quasiparticle self-consistent *GW* method: A basis for the independent-particle approximation, *Phys. Rev. B* **76**, 165106 (2007).
- [23] T. Kotani, Quasiparticle Self-Consistent *GW* Method Based on the Augmented Plane-Wave and Muffin-Tin Orbital Method, *Journal of the Physical Society of Japan* **83**, 094711 (2014).
- [24] L. Hedin and S. Lundqvist, *Effects of Electron-Electron and Electron-Phonon interactions on the One-Electron States of Solids*, Vol. 12 (Oxford university press New York, 1969).
- [25] F. Aryasetiawan and O. Gunnarsson, The *GW* method, *Reports on Progress in Physics* **61**, 237 (1998).
- [26] A. L. Kutepov, Electronic structure of Na, K, Si, and LiF from self-consistent solution of Hedin’s equations including vertex corrections, *Phys. Rev. B* **94**, 155101 (2016).
- [27] M. S. Hybertsen and S. G. Louie, Electron correlation in semiconductors and insulators: Band gaps and quasipar-

- ticle energies, Phys. Rev. B **34**, 5390 (1986).
- [28] M. Shishkin, M. Marsman, and G. Kresse, Accurate Quasiparticle Spectra from Self-Consistent *GW* Calculations with Vertex Corrections, Phys. Rev. Lett. **99**, 246403 (2007).
- [29] H. Sakakibara, T. Kotani, M. Obata, and T. Oda, Finite electric-field approach to evaluate the vertex correction for the screened coulomb interaction in the quasiparticle self-consistent *GW* method, Phys. Rev. B **101**, 205120 (2020).
- [30] M. van Schilfgaarde, T. Kotani, and S. Faleev, Quasiparticle Self-Consistent *GW* Theory, Phys. Rev. Lett. **96**, 226402 (2006).
- [31] S. Botti and M. A. L. Marques, Strong Renormalization of the Electronic Band Gap due to Lattice Polarization in the *GW* Formalism, Phys. Rev. Lett. **110**, 226404 (2013).
- [32] C. Bhandari, M. van Schilfgaarde, T. Kotani, and W. R. L. Lambrecht, All-electron quasiparticle self-consistent *GW* band structures for SrTiO₃ including lattice polarization corrections in different phases, Phys. Rev. Materials **2**, 013807 (2018).
- [33] A. N. Chantis, M. van Schilfgaarde, and T. Kotani, Ab Initio Prediction of Conduction Band Spin Splitting in Zinc Blende Semiconductors, Phys. Rev. Lett. **96**, 086405 (2006).
- [34] J. He and C. Franchini, Screened hybrid functional applied to $3d^0 \rightarrow 3d^8$ transition-metal perovskites LaMO₃ ($M=\text{Sc-Cu}$): influence of the exchange mixing parameter on the structural, electronic and magnetic properties, Physical Review B **86**, 235117 (2012), arXiv: 1209.0486.
- [35] A. A. Mostofi, J. R. Yates, Y.-S. Lee, I. Souza, D. Vanderbilt, and N. Marzari, WANNIER90: A tool for obtaining maximally-localised Wannier functions, Computer Physics Communications **178**, 685 (2008).
- [36] A. A. Mostofi, J. R. Yates, G. Pizzi, Y.-S. Lee, I. Souza, D. Vanderbilt, and N. Marzari, An updated version of WANNIER90: A tool for obtaining maximally-localised Wannier functions, Computer Physics Communications **185**, 2309 (2014).
- [37] M. A. McGuire, H. Dixit, V. R. Cooper, and B. C. Sales, Coupling of Crystal Structure and Magnetism in the Layered, Ferromagnetic Insulator CrI₃, Chemistry of Materials **27**, 612 (2015).
- [38] V. Carteaux, D. Brunet, G. Ouvrard, and G. Andre, Crystallographic, magnetic and electronic structures of a new layered ferromagnetic compound Cr₂Ge₂Te₆, Journal of Physics: Condensed Matter **7**, 69 (1995).
- [39] H.-J. Deiseroth, K. Aleksandrov, C. Reiner, L. Kienle, and R. K. Kremer, Fe₃GeTe₂ and Ni₃GeTe₂ Two New Layered Transition-Metal Compounds: Crystal Structures, HRTEM Investigations, and Magnetic and Electrical Properties, European Journal of Inorganic Chemistry **2006**, 1561 (2006).
- [40] A. I. Liechtenstein, V. I. Anisimov, and J. Zaanen, Density-functional theory and strong interactions: Orbital ordering in Mott-Hubbard insulators, Phys. Rev. B **52**, R5467 (1995).
- [41] A. G. Petukhov, I. I. Mazin, L. Chioncel, and A. I. Liechtenstein, Correlated metals and the LDA+*U* method, Phys. Rev. B **67**, 153106 (2003).
- [42] J. P. Perdew, K. Burke, and M. Ernzerhof, Generalized Gradient Approximation Made Simple, Phys. Rev. Lett. **77**, 3865 (1996).
- [43] T. Kotani and H. Kino, Re-examination of half-metallic ferromagnetism for doped LaMnO₃ in a quasiparticle self-consistent *GW* method, Journal of Physics: Condensed Matter **21**, 266002 (2009).
- [44] S. W. Jang, T. Kotani, H. Kino, K. Kuroki, and M. J. Han, Quasiparticle self-consistent *GW* study of cuprates: electronic structure, model parameters, and the two-band theory for T_C , Scientific Reports **5**, 12050 (2015).
- [45] See Supplemental Material for more detailed band structures and density of states calculated using various methods.
- [46] P. Janthon, S. A. Luo, S. M. Kozlov, F. Vies, J. Limtrakul, D. G. Truhlar, and F. Illas, Bulk Properties of Transition Metals: A Challenge for the Design of Universal Density Functionals, Journal of Chemical Theory and Computation **10**, 3832 (2014).
- [47] Y. Meng, X.-W. Liu, C.-F. Huo, W.-P. Guo, D.-B. Cao, Q. Peng, A. Dearden, X. Gonze, Y. Yang, J. Wang, H. Jiao, Y. Li, and X.-D. Wen, When Density Functional Approximations Meet Iron Oxides, Journal of Chemical Theory and Computation **12**, 5132 (2016).
- [48] H. Wang, V. Eyert, and U. Schwingenschlgl, Electronic structure and magnetic ordering of the semiconducting chromium trihalides CrCl₃, CrBr₃, and CrI₃, Journal of Physics: Condensed Matter **23**, 116003 (2011).
- [49] J. F. Dillon and C. E. Olson, Magnetization, Resonance, and Optical Properties of the Ferromagnet CrI₃, Journal of Applied Physics **36**, 1259 (1965).
- [50] Y. F. Li, W. Wang, W. Guo, C. Y. Gu, H. Y. Sun, L. He, J. Zhou, Z. B. Gu, Y. F. Nie, and X. Q. Pan, Electronic structure of ferromagnetic semiconductor CrGeTe₃ by angle-resolved photoemission spectroscopy, Phys. Rev. B **98**, 125127 (2018).
- [51] M. Suzuki, B. Gao, K. Koshiishi, S. Nakata, K. Hagiwara, C. Lin, Y. X. Wan, H. Kumigashira, K. Ono, S. Kang, S. Kang, J. Yu, M. Kobayashi, S.-W. Cheong, and A. Fujimori, Coulomb-interaction effect on the two-dimensional electronic structure of the van der Waals ferromagnet Cr₂Ge₂Te₆, Phys. Rev. B **99**, 161401 (2019).
- [52] H. Ji, R. A. Stokes, L. D. Alegria, E. C. Blomberg, M. A. Tanatar, A. Reijnders, L. M. Schoop, T. Liang, R. Prozorov, K. S. Burch, N. P. Ong, J. R. Petta, and R. J. Cava, A ferromagnetic insulating substrate for the epitaxial growth of topological insulators, Journal of Applied Physics **114**, 114907 (2013).
- [53] C. Ricca, I. Timrov, M. Cococcioni, N. Marzari, and U. Aschauer, Self-consistent DFT+*U*+*V* study of oxygen vacancies in SrTiO₃ (2020), arXiv:2001.06540 [cond-mat.mtrl-sci].
- [54] A. L. Kutepov, Self-consistent *GW* method: $O(N)$ algorithm for the polarizability and the self energy (2019), arXiv:1911.05633 [cond-mat.mtrl-sci].

SUPPLEMENTAL

1. Band structures and Density of States calculated in DFT and QSGW

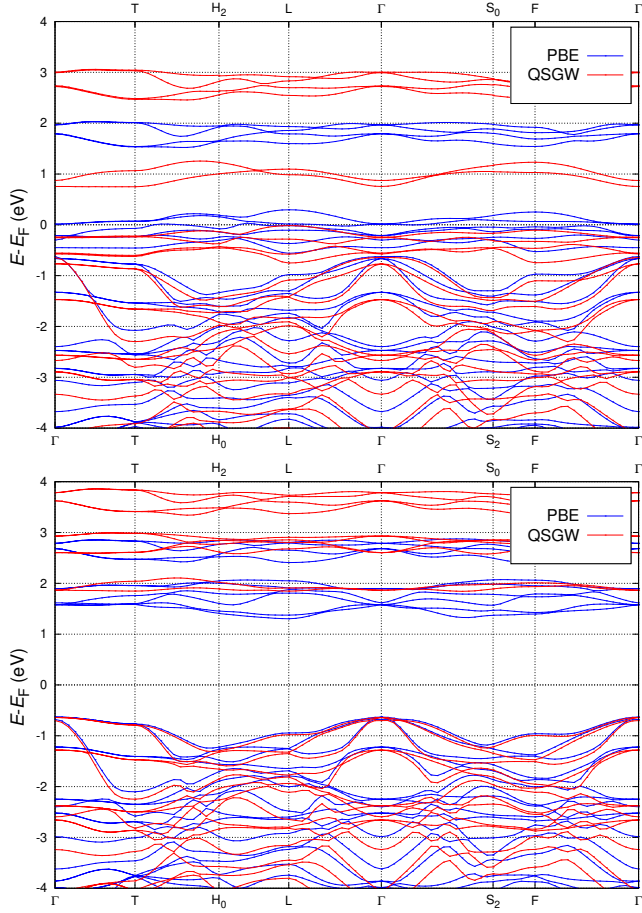
a. VI_3 

FIG. S1. Spin-polarized band structures of VI_3 . The top (bottom) panel shows the majority (minority) spin state. For comparison, QSGW (red) and PBE (blue) results are shown on the same panel.

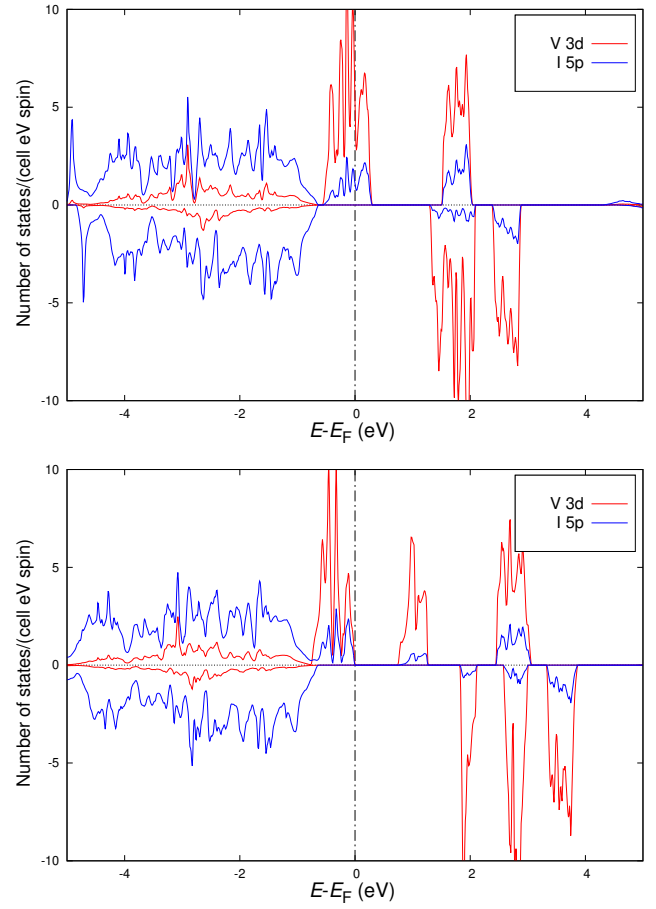


FIG. S2. The partial density of states projected on V-3d and I-5p states in VI_3 . The top (bottom) panel shows DFT-PBE (QSGW) results. DFT can not open a gap and result in a metallic state. Within QSGW, the minority spin channel has a much larger bandgap than the majority spin channel.

b. CrGeTe₃

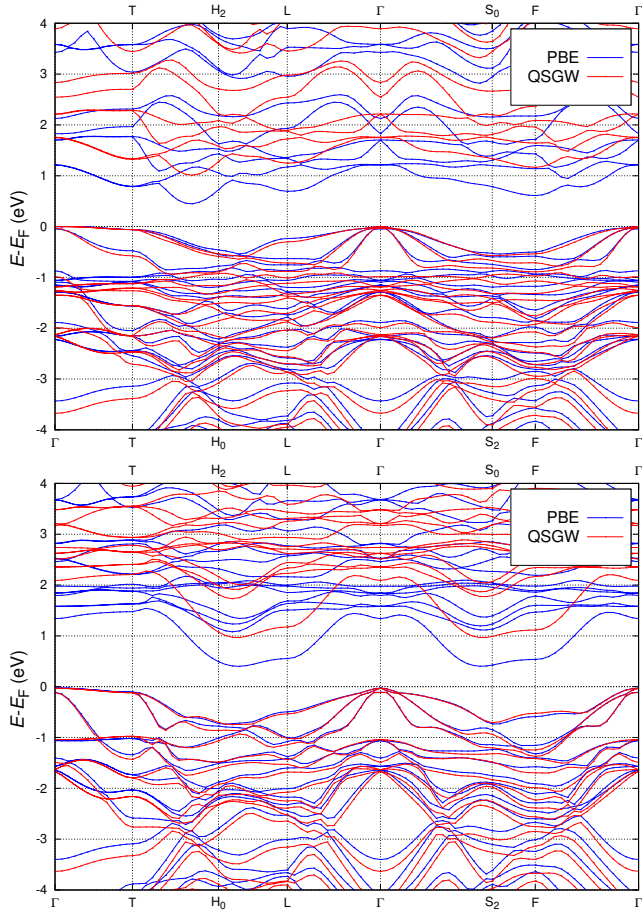


FIG. S3. Spin-polarized band structures of CrGeTe₃ calculated in DFT and QSGW. The top (bottom) panel shows the majority (minority) spin state.

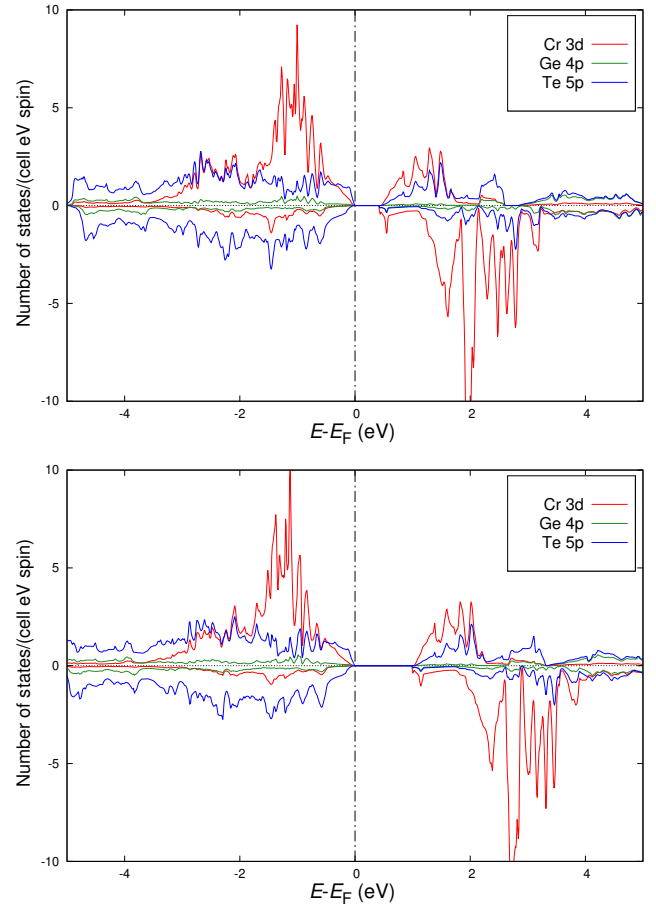


FIG. S4. The partial density of states projected on Cr-3d, Ge-4p, and Te-5p states in CrGeTe₃ calculated in DFT-PBE (top) and QSGW (bottom).

c. Fe_3GeTe_2

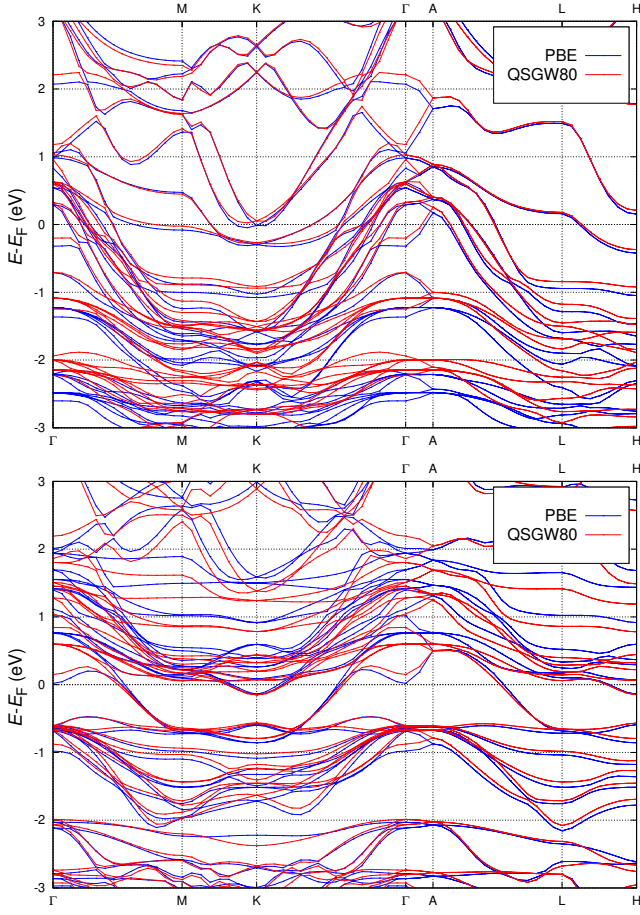


FIG. S5. Spin-polarized band structures of Fe_3GeTe_2 calculated in DFT and QSGW. The top (bottom) panel shows the majority (minority) spin state.

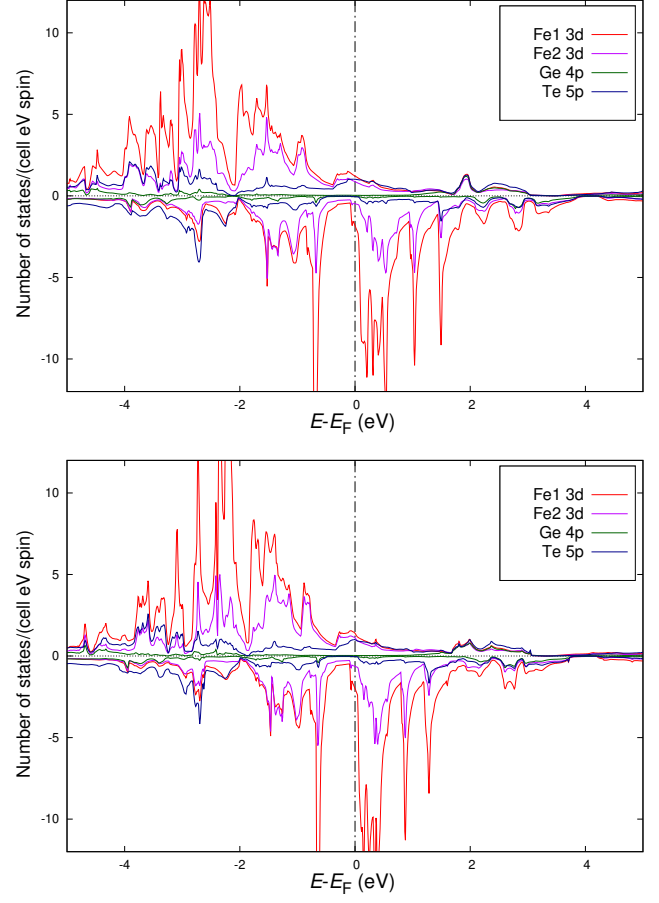


FIG. S6. The partial density of states projected on Fe-3d, Ge-4p, and Te-5p states in Fe_3GeTe_2 calculated in DFT (top) and QSGW (bottom).

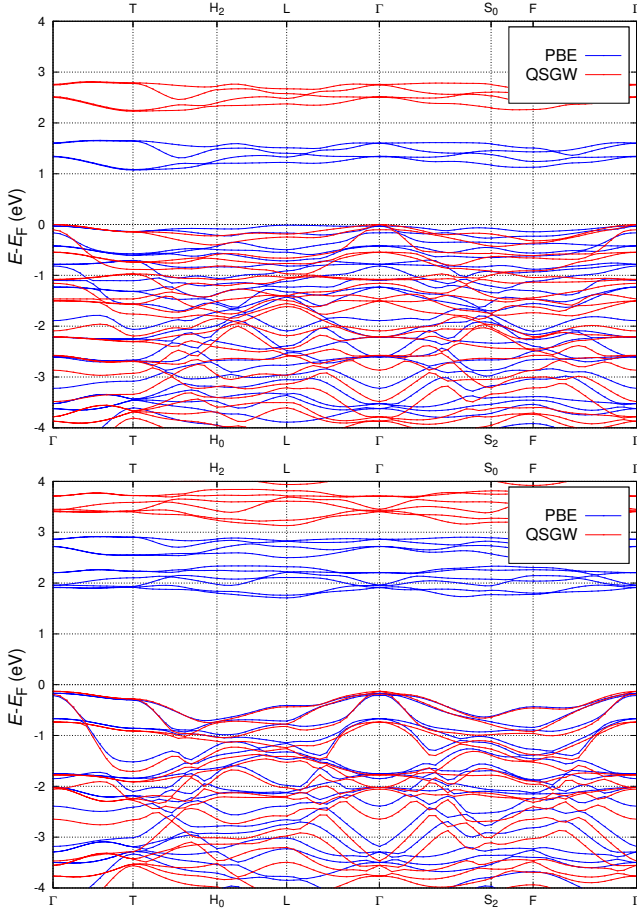
d. CrI_3 

FIG. S7. Spin-polarized band structures of CrI_3 calculated in DFT and QSGW. The top (bottom) panel shows the majority (minority) spin state. QSGW shifts the unoccupied states up and increases the bandgap.

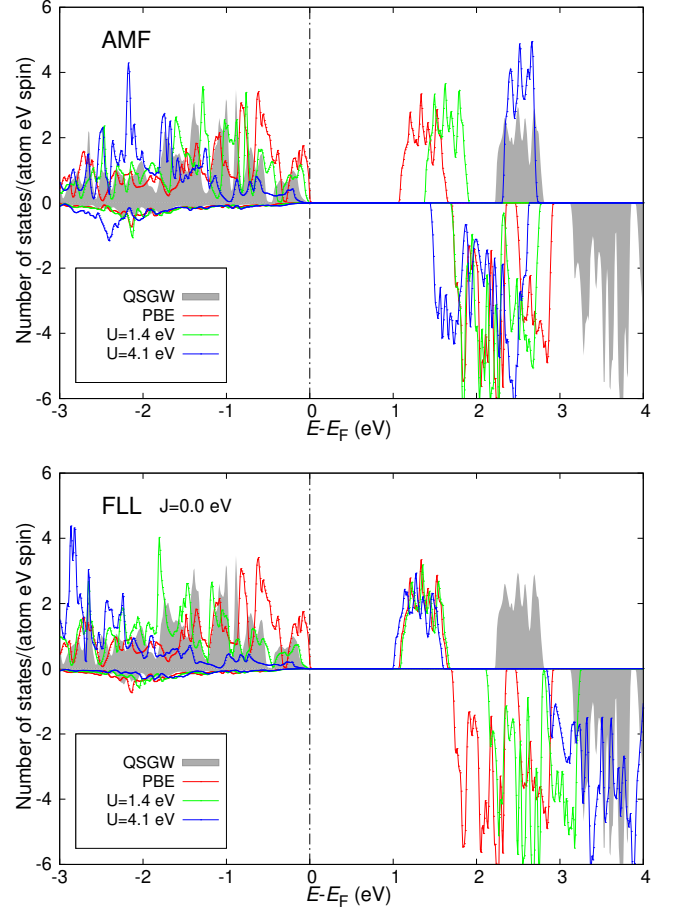
2. DOS calculated in DFT+ U , DFT, and QSGWa. CrI_3 

FIG. S8. The partial density of states projected on Cr-3d states in CrI_3 . Both AMF (top) and FLL (bottom) double-counting schemes are employed for the DFT+ U calculations.

b. CrGeTe_3

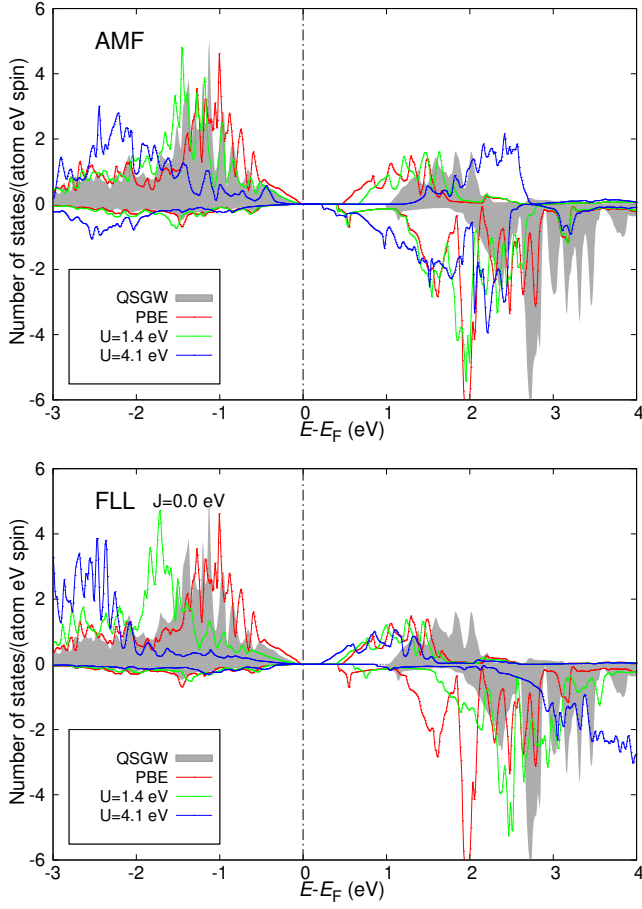


FIG. S9. The partial density of states projected on Cr- $3d$ states in CrGeTe_3 . Both AMF (top) and FLL (bottom) double-counting schemes are employed for the DFT+ U calculations.

c. VI_3

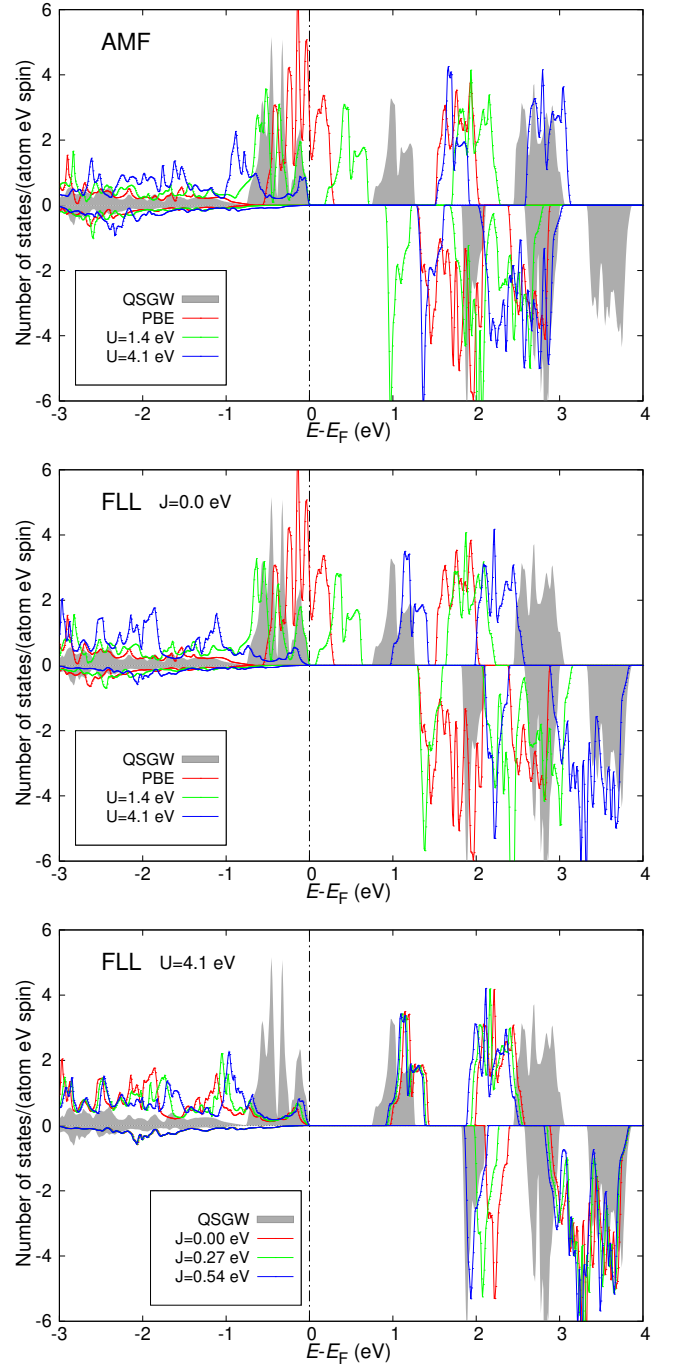


FIG. S10. The partial density of states projected on V- $3d$ states. The top panel shows DFT+ U results calculated using the AMF scheme. DFT+ U calculations in the middle and bottom panel are carried out using the FLL scheme. The middle panel is calculated using various U values and $J = 0 \text{ eV}$. The bottom panel is calculated using various J values and $U = 4.1 \text{ eV}$.